J Mater Sci (2014) 49:5529–5536
DOI 10.1007/s10853-014-8242-z

Doping-induced electron density modification at lattice sites of ZnO:Ga nanostructures: effects on vibrational and optical properties

S. Saravanakumar · A. Escobedo-Morales · U. Pal · R. J. Aranda · R. Saravanan

Received: 2 December 2013 / Accepted: 10 April 2014 / Published online: 14 May 2014

Abstract Effects of Ga doping on the morphology, microstructure, electron density distribution, and optical properties of hydrothermally grown ZnO nanostructures have been studied by means of scanning electron microscopy, diffuse reflectance spectroscopy, X-ray diffraction, and the maximum entropy methods. It has been shown that while Ga incorporation in ZnO lattice does not result in a large distortion of its wurtzite structure, it affects substantially the electronic charge distribution along the Zn–O bonds. Anisotropic redistribution of the electron charge density around the cation sites consolidates the assumption that the Ga atoms in doped nanostructures incorporate by substituting Zn atoms. The formation of a high density of point defects modifies the lattice dynamics of ZnO; in addition, it introduces a pronounced band-tail in the forbidden band gap.

S. Saravanakumar (✉) · R. Saravanan
Research Centre and PG Department of Physics, The Madura College, Madurai 625011, Tamil Nadu, India
e-mail: saravanaphysics@gmail.com

A. Escobedo-Morales
Facultad de Ingeniería Química, Benemérita Universidad Autónoma de Puebla, 72570 Puebla, Pue., Mexico

U. Pal
Instituto de Física, Benemérita Universidad Autónoma de Puebla, Apdo. Postal J-48, 72570 Puebla, Pue., Mexico

R. J. Aranda
Centro de Investigaciones en Dispositivos Semiconductores, Benemérita Universidad Autónoma de Puebla, 72570 Puebla, Pue., Mexico

Introduction

Zinc oxide (ZnO) is an *n*-type wide band gap semiconductor (3.37 eV at room temperature) vastly used for the development of optoelectronic devices like light-emitting devices and solar cells [1]. Non-intentionally doped ZnO gives *n*-type conduction with a typical carrier concentration of $\sim 10^{17}$ cm^{-3} [2, 3], which, although high, is far below the required carrier concentrations for laser diode applications. Hence, controlling the carrier concentration of ZnO remains a major challenge for its optoelectronic applications. In this effect, IIIA elements such as B, Al, Ga, and In have been utilized as *n*-type dopants to increase the carrier concentration of ZnO as high as 10^{21} cm^{-3} [4–8]. Among them, Ga seems to be the most effective *n*-type dopant in ZnO [9], as the bond length of Ga–O (1.92 Å) is nearly equal to that of Zn–O (1.97 Å) [10]. On the other hand, the interest in low-dimensional ZnO structures has increased drastically in recent years due to the novel physical properties they exhibit. For example, it is believed that doped *n*-type ZnO nanostructures with high carrier concentrations have potential for diverse applications, including microelectronics, chemical and biological sensing and diagnosis, energy conversion and storage, light-emitting displays, catalysis, drug delivery, and optical storage [11–13]. However, for each of these applications, controlling the carrier concentration or, specifically, the electron charge distribution is extremely important for acquiring desired effects in the fabricated devices, since any chemical or physical process happens ultimately, through the interaction of electrons of the atoms/ions in crystal lattice. Hence, elucidating the properties like electron distribution and charge ordering in crystal lattice is a pivotal issue for the utilization of doped nanocrystals. Nevertheless, despite its relevance, to the best of our

knowledge, detailed studies concerning spatial charge redistribution induced by doping process have not been reported for ZnO nanostructures.

In the present work, the effect of gallium content on the spatial distribution of electronic charge, along with its consequences over the structural and optical properties of hydrothermally grown ZnO nanostructures is studied experimentally using powder X-ray diffraction, Rietveld refinement [14, 15], and maximum entropy method [16]. Effects of Ga inclusion on the charge distribution and bonding behavior of constituent atoms in ZnO lattice have been analyzed. The morphology, elemental composition, vibrational modes, and optical characteristics of the samples have been studied using scanning electron microscopy, energy dispersive X-ray spectroscopy, Raman spectroscopy, and diffuse reflectance spectroscopy techniques.

Experimental

The gallium-doped ZnO samples were synthesized through a low-temperature hydrothermal route. Briefly, zinc acetate dihydrate($Zn(CH_3COO)_2{\cdot}2H_2O$; J.T. Baker, 99.9 %), gallium (III) nitrate hydrate ($Ga(NO_3)_3{\cdot}xH_2O$; Aldrich, 99.99 %), sodium hydroxide (NaOH; J.T. Baker, 99.9 %), and ethylenediamine ($H_2N(CH_2)_2NH_2$, EDA; J.T. Baker, 99.9 %) were used as received. In a typical synthesis, an alkaline solution was prepared dissolving 15 mL of EDA in 135 mL of ultrapure deionized water (resistivity $>$ 18 MΩ cm) under vigorous magnetic stirring. Then, 12.8 g of zinc acetate was added to the previous solution until the solution become optically transparent. The pH of the solution was then adjusted to 12 by adding about 2.12 g of NaOH. The temperature of the mixture solution was then increased up to 100 °C and maintained at this temperature for 15 h. Finally, the solution was freely cooled to room temperature, and the obtained precipitate was filtered and dried under vacuum. For obtaining Ga-doped ZnO nanostructures, keeping all conditions same as undoped sample, 50.3, 127.6, and 261.9 mg of gallium nitrate were dissolved in the reaction solution before the thermal treatment to obtain nominally 1.0, 2.5, and 5.0 mol% doped samples, respectively.

Doped and undoped samples were analyzed through scanning electron microscopy, energy dispersive X-ray spectroscopy (SEM/EDS; Jeol JSM 6610LV with an Oxford Instruments INCA X-Act EDS analytical system attached), powder X-ray diffraction (XRD; Philips X'Pert PRO), Raman spectroscopy (LabRAM HR-Olympus system in backscattering configuration, $\lambda_{exc} = 633$ nm), and diffuse reflectance spectroscopy (DRS; Varian Cary 5000). The crystal structure and charge density were analyzed further through the Rietveld refinement and the maximum entropy method (MEM).

Results and discussion

Figure 1 shows typical SEM micrographs of the undoped and doped samples. For the undoped sample (Fig. 1a), formation of microstructures constituting a radial arrangement of needle-like nanostructures is observed. Such structural sub-units are around 200 nm in diameter and about 6 microns in length. Formation of observed morphology suggests an agglomeration of ZnO nuclei at the very early stage of growth process. It can be noted that as the nominal Ga content increases, the morphology of the one-dimensional primary structures changes progressively from needle-like to rod-like (Fig. 1b–d). For the 5.0 % nominal Ga-doped ZnO sample, a rough structure localized at the tip of the nanostructures is observed. A depletion of available ZnO growth units along with an increase of the Ga/Zn ratio at the final stages of growth process was found responsible for such peculiar feature [17].

The elemental composition of the synthesized samples determined by EDS is presented in Table 1. It can be seen that the average Ga atom percent (at.%) does not follow a linear tendency; nevertheless, it increases monotonically with the nominal content in the samples. EDS results of the doped samples suggest that most of the Ga atoms incorporate into the ZnO lattice as substitutional defects (Ga_{Zn}), since the O at.% remains almost same and Zn at.% decreases with the increase of Ga content in the reaction mixture. Probably, formation of positively charged point defects (e.g., O_i or V_{Zn}) to retain the local electroneutrality near to Ga_{Zn} contributes with the observed lower metallic ion concentration for heavily doped samples [9, 18].

Both the doped and undoped ZnO nanostructures were characterized by powder X-ray diffraction. The diffraction intensity data were collected using an X'Pert PRO (Philips, the Netherlands) X-ray diffractometer set in Bragg–Brentano (θ–2θ) geometry equipped with a monochromatic source of Cu K_α radiation (mixture of Cu $K_{\alpha1}$ and Cu $K_{\alpha2}$; $\lambda = 1.5418$ Å). The X-ray patterns were acquired in the 2θ range of 10°–120° with a step size of 0.02°. Figure 2 shows the X-ray diffraction patterns of the ZnO nanostructures with different gallium contents. For the doped and undoped samples, all the observed diffraction peaks match with the standard X-ray powder diffraction pattern reported for wurtzite ZnO phase (*w*-ZnO) [19]. No additional diffraction signal attributable to a secondary phase was identified. It can be seen that the Ga doping has no strong influence on the intensity and width of the ZnO diffraction peaks. Therefore, it is proposed that the incorporated Ga atoms occupy preferential sites in the ZnO lattice, preventing any significant lattice disorder. Because of its size and valency, most of the incorporated gallium atoms get incorporated into the ZnO lattice mostly as substitutional defects (Ga_{Zn}), in agreement with the EDS results. Although, it is expected

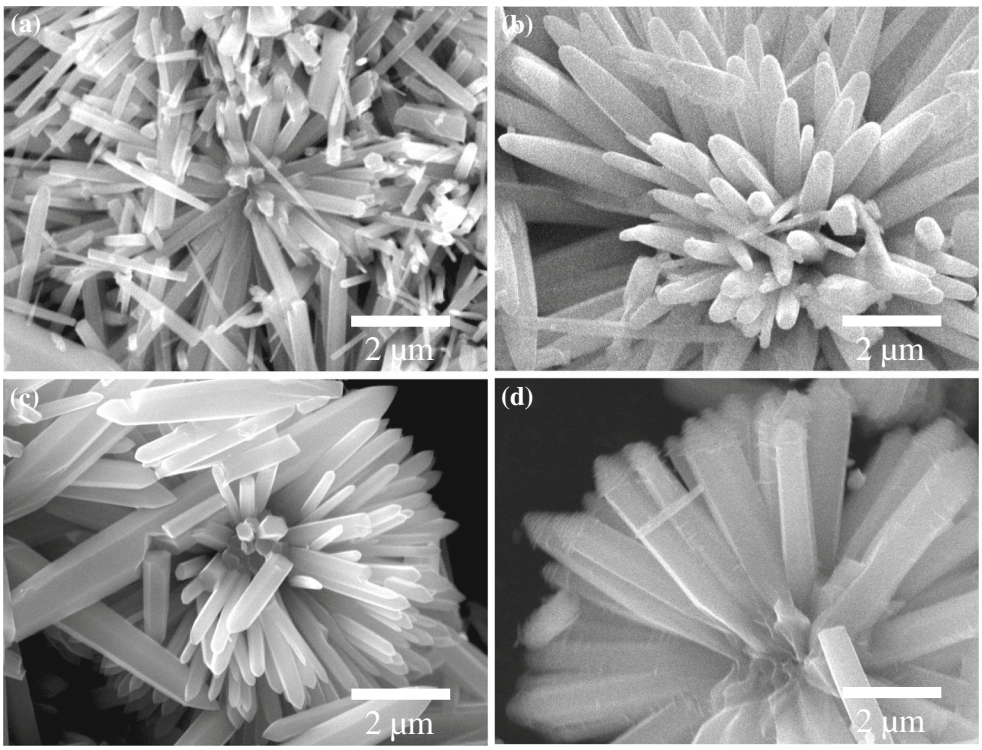

Fig. 1 Typical SEM micrographs of the **a** undoped, **b** 1.0, **c** 2.5, and **d** 5.0 mol% (nominal) Ga-doped samples

Table 1 EDS elemental composition, estimated band gap energy (E_g), and band-tail parameter (E_0) of undoped and gallium-doped samples

Nominal Ga concentration (mol%)	Zn:O:Ga (at.%, average)	E_g (eV)	E_0 (meV)
0.0	47.73:52.27:0.00	3.24(3)	75
1.0	46.90:52.95:0.15	3.24(2)	95
2.5	50.16:49.55:0.29	3.31(2)	105
5.0	40.44:58.47:1.08	3.30(3)	100

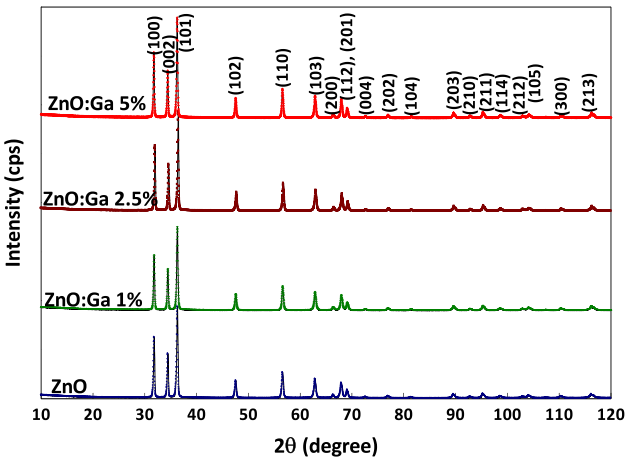

Fig. 2 X-ray powder diffraction patterns of the doped and undoped samples

that under high doping concentrations, interstitial Ga defects (Ga_i) could be formed, nevertheless formation of such defects is energetically less favorable than substitutional Ga. Therefore, the point defects like Ga_{Zn} must dominate in the nanocrystals until the concentration of incorporated gallium is below its solubility limit [20, 21].

The effect of Ga content on the structural features of ZnO nanostructures was analyzed further using the Rietveld refinement method [14]. JANA 2006 software [22] was used to fit the experimental and calculated diffraction patterns by considering the hexagonal structure of *w*-ZnO, which belongs to the $P6_3mc$ space group containing two formula units per primitive cell. The input atomic coordinates (x, y, z) were set as $\left(\frac{1}{3}, \frac{2}{3}, 0\right)$ and $\left(\frac{2}{3}, \frac{1}{3}, \frac{1}{2}\right)$ for Zn atoms, and $\left(\frac{1}{3}, \frac{2}{3}, u\right)$ and $\left(\frac{2}{3}, \frac{1}{3}, u + \frac{1}{2}\right)$ for O atoms, where $u = 0.3875$ [23, 24]. The experimental and calculated XRD patterns for the undoped and doped samples are shown in Fig. 3. Reliability indices and other refined parameters are summarized in Table 2. It can be noted that initially the lattice parameters *a* and *c* tend to lengthen with Ga content and therefore also the unit cell volume. The lattice parameter may not be linear after about 2.5 % of Ga^{3+} doping. This structural feature of doped samples can be attributed to a high density of Ga atoms located at Zn sites and the formation of interstitial oxygen (O_i) [21]. However, for the

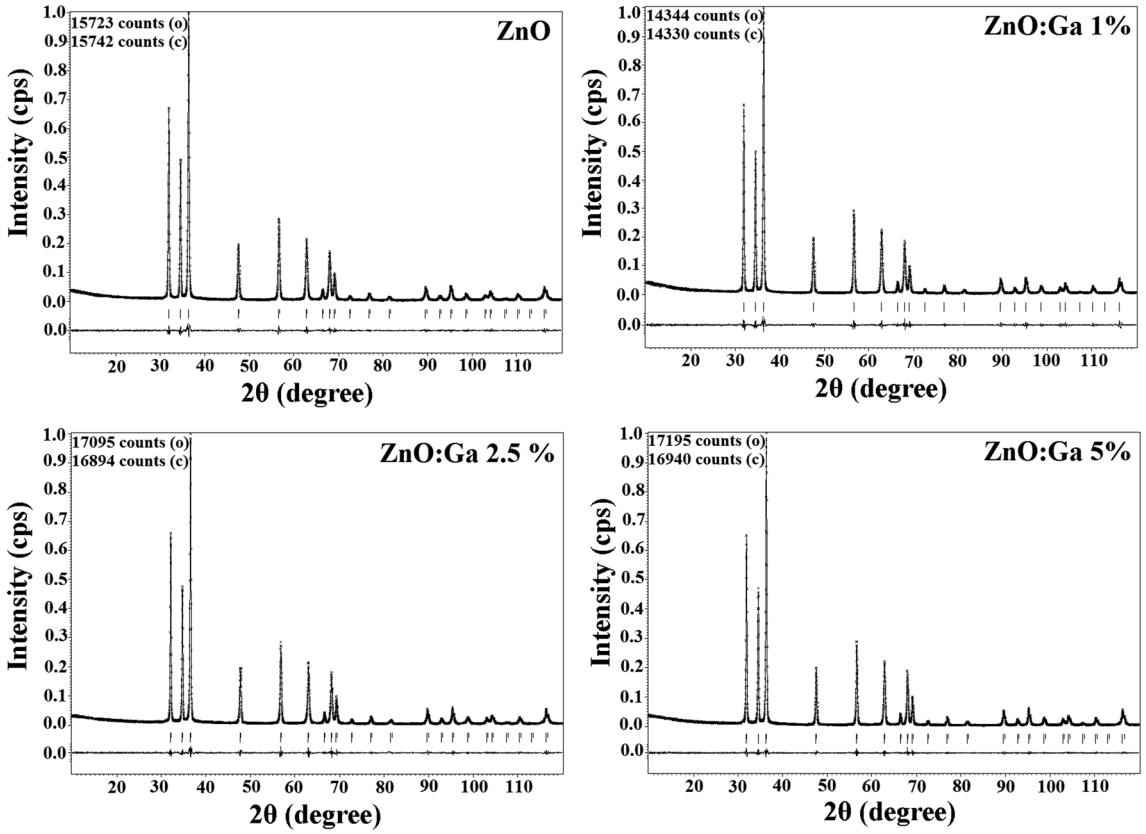

Fig. 3 Observed (*circles*) and calculated (*continuous line*) XRD patterns of the undoped and Ga-doped samples. The *vertical bars* indicate the *w*-ZnO reflection positions. The *difference plot* is shown at the *bottom* for each sample

Table 2 Refined structural parameters for undoped and gallium-doped samples

Refined parameter	Nominal Ga concentration (mol%)			
	0.0	1.0	2.5	5.0
a (Å)	3.2487 (15)	3.2496 (14)	3.2412 (41)	3.2503 (8)
c (Å)	5.2033 (29)	5.2036 (26)	5.1943 (77)	5.2059 (14)
$\alpha = \beta$	90°	90°	90°	90°
γ	120°	120°	120°	120°
Volume (Å^3)	47.5585 (453)	47.5886 (417)	47.2567 (1250)	47.6304 (223)
R_{obs} (%)	0.81	0.67	0.54	0.78
R_p (%)	4.90	5.52	5.03	4.40
B_{Zn} (Å^2)	1.0184	1.0389	1.1022	1.0103
B_O (Å^2)	0.7651	0.8961	0.8409	0.7767

2.5 % (nominal)-doped sample, the unit cell volume shrinks with respect to the undoped sample, indicating the presence of compressive strain [25]. Such behavior could be attributed to the formation of zinc vacancies (V_{Zn}) generated to maintain the local charge neutrality, as the Ga content increases further. Furthermore, the isotropic Debye–Waller factors of Zn (B_{Zn}) and O (B_O) atoms follow similar behavior, probably due to static distortion caused by the incorporated Ga ions of larger radius. The B values of Ga^{3+}-doped ZnO nanostructures are slightly large compared to those of pure ZnO as seen from Table 2. This may be due to the fact that there might be inhomogeneous distribution of Ga^{3+} during growth using wet chemical synthesis.

The grain size of the undoped and gallium-doped ZnO nanostructures was estimated from the observed full width at half maximum of their XRD peaks using GRAIN software [26]. The average grain size of the nanostructures was estimated to be about 25 nm, corresponding to approximately eight coherently diffracting domains in each particle [27]. The number of coherently diffracting domains was calculated using the relation $N = r_{SEM}/r_{X\text{-}ray}$, where N is the number of coherently diffracting domains, r_{SEM} is the average length of the crystals estimated through SEM images, and $r_{X\text{-}ray}$ is the average grain size calculated from the XRD peak profiles.

Maximum entropy method (MEM) [16] is an exact and versatile tool to determine the electron density distribution of crystalline structures. This method needs minimum

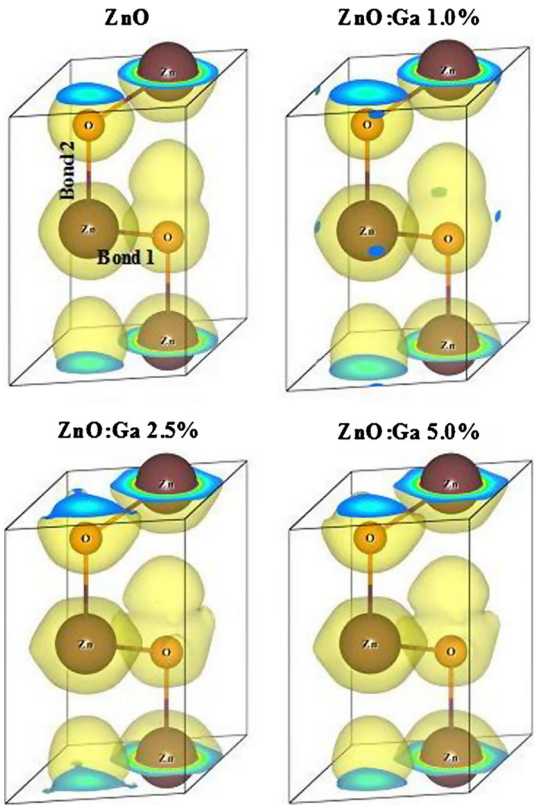

Fig. 4 3D electron density for the undoped and Ga-doped samples (isosurface: 0.52 e/Å^3)

information to determine the spatial electron density distribution in a solid crystal with high accuracy based on probabilistic approaches, yielding the least biased information. The only limitation of the method is the computing power of the machine on which it runs. Since the electron density is being refined cyclically in each generated pixel (e.g., in the present work, the primitive cell of the ZnO has been divided into $32 \times 32 \times 48$ pixels), in most of the cases, a supercomputing system is needed for analyzing lower symmetry crystallographic systems. In this work, the software package PRIMA [28] was used for MEM computations, and the obtained results were visualized using the software VESTA [29].

Three-dimensional (3D) electron density distributions of the ZnO:Ga systems with different Ga contents are shown in Fig. 4, considering the isosurface level of 0.52 e/Å^3 for all of them. It can be seen that the cross section of the electron density around the cation sites changes progressively with Ga content. However, the main effect of the Ga doping is a notorious increase of the volume of electron density around oxygen sites probably due to the truncation in the experimental number of measured Bragg peaks. Moreover, the present analysis is based on powder data sets, and hence, averaging of equivalent Bragg reflections might have taken place. The above factors give rise to slight elongation in electron density along *c*-axis. But, we tend to compare the electron densities computed using similar model parameters, and hence this can be justified.

Figure 5 shows two-dimensional (2D) electron density maps corresponding to the doped and undoped samples. The demonstrated planes are parallel to the (100), (110) and (014) crystallographic planes, situated 2.816, 1.625, and 2.68 Å away from the origin of the primitive cell, respectively. The 2D maps reveal that although the cation coordination polyhedra are nearly regular tetrahedrons, the effect of Ga doping on electron distribution is anisotropic. While the bond 1 (108° to the *c*-axis, see Fig. 4) progressively develops a polar-covalent character, the bond 2 (parallel to *c*-axis, see Fig. 4) gets more ionic as the Ga content increases. This behavior can be explained considering the wurtzite structure of ZnO. It is proposed that the extra valence electrons introduced by Ga_{Zn} defects migrate toward the nearest O-plane, increasing the electron density along the bond 1. A smaller difference between Ga–O electronegativities than Zn–O facilitates such electron transfer, inducing a covalent character in bond 1. On the other hand, a lower electron density in the O-planes is expected to increase the polar strength along the [001] axis, making the bond 2 more ionic with the increase of Ga content (as seen from Table 3). Detailed quantitative information concerning the redistribution of electron density along the bond 1 and bond 2 directions are provided in the one-dimensional electron density profiles shown in Fig. 6. The electron densities at the midpoint of both the characteristic Zn–O bonds (bond 1 and bond 2) clearly demonstrate their inverse variation on Ga doping. The calculated mid-bond electron density values are summarized in Table 3 for comparison.

It is clear that a redistribution of the electron density between cations and anions will influence the physical properties of materials. Among them, the vibrational properties, i.e., the phonon modes, are highly sensitive to bond strength [30, 31] determined by the electron density and disturbances in the lattice arrangement [32]. Therefore, Raman spectroscopy could provide valuable information that can be directly related with the formation of lattice defects and changes in electron density due to doping process. Figure 7 shows the Raman spectra of the undoped and gallium-doped samples. For the undoped sample, fundamental phonon modes related to *w*-ZnO structure such as E_{2L} (101 cm^{-1}), A_{1T} (380 cm^{-1}), and E_{2H} (440 cm^{-1}), along with the second-order modes 2-E_{2L} (204 cm^{-1}) and E_{2H}–E_{2L} (334 cm^{-1}) [17, 24] are clearly recognized. The observed sharp peaks suggest that undoped ZnO nanostructures do not contain considerable amount of lattice defects. However, as the Ga content increases, the Raman peaks get broadened, and their

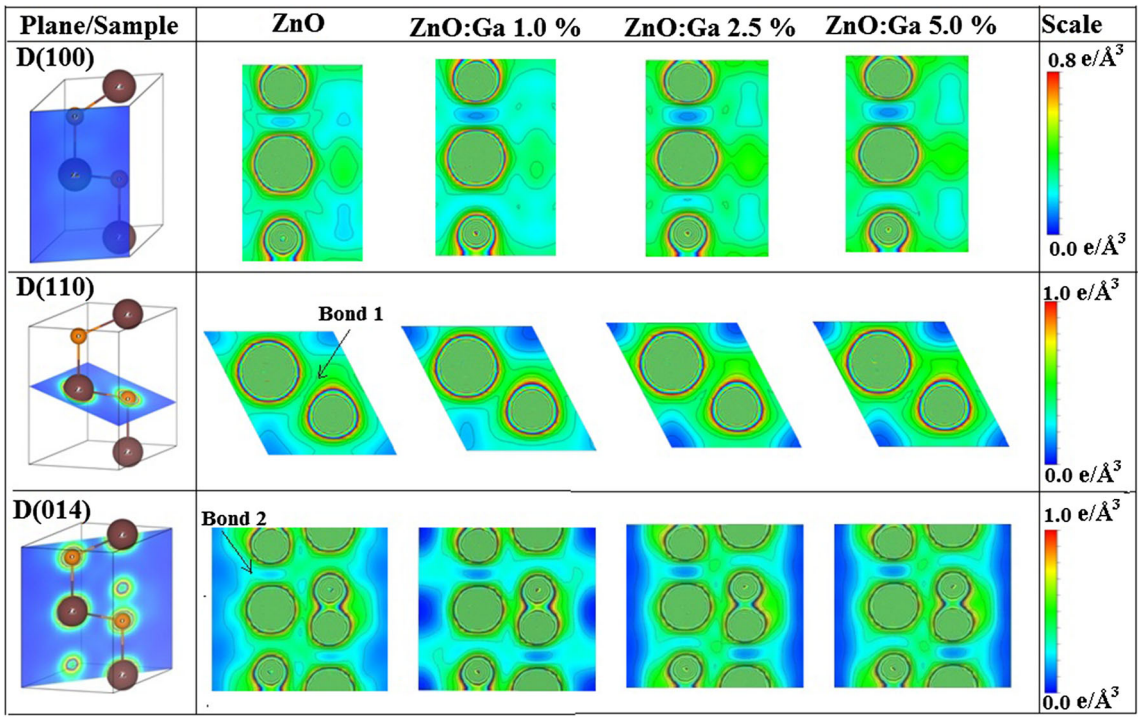

Fig. 5 2D electron density maps drawn parallel to (100), (014), and (110) crystallographic planes of undoped and Ga-doped ZnO samples

Table 3 Calculated bond lengths and mid-bond electron density for Zn–O bond along the bond 1 and bond 2 directions for the doped and undoped samples

Nominal Ga concentration (mol%)	Bond 1		Bond 2	
	Bond length (Å)	Mid-bond electron density (e/Å^3)	Bond length (Å)	Mid-bond electron density (e/Å^3)
0.0	2.0980	0.3872	2.1824	0.2029
1.0	2.0982	0.4443	2.1652	0.1460
2.5	2.1398	0.4195	2.1796	0.1383
5.0	2.1158	0.4217	2.1640	0.1376

intensity decreases considerably, suggesting the formation of lattice defects associated with the incorporated Ga atoms. It can be noted further that the Raman spectra of the Ga-doped samples present a broad background in the range of 300–600 cm^{-1}. It is attributed to fluorescence coming from the samples.

Wang et al. [33] and Windisch et al. [34] have suggested that intrinsic mixing of two different cations via doping may induce charge redistribution and therefore changes of the local polarizability; as a result, the scattering cross section of at least one vibrational mode could be strongly influenced. The inset of Fig. 7 shows the effect of Ga content on the Raman peaks assigned to the fundamental E_2 modes of *w*-ZnO. Although as light red-shift (lower frequency) of both the peaks is observed due to Ga doping, the main effect is the quench of the Raman signal of E_{2H}

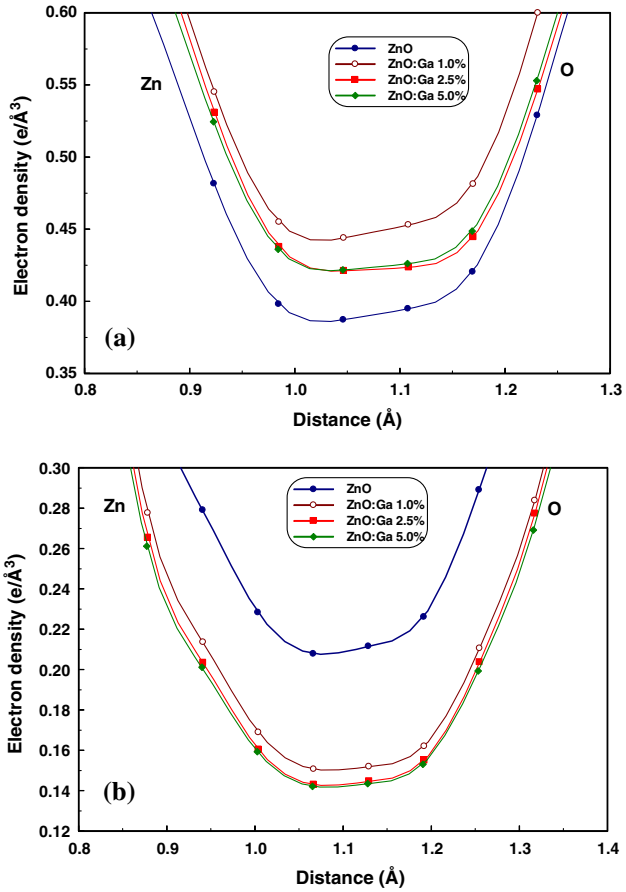

Fig. 6 One-dimensional electron density profiles for the samples along the **a** bond 1 **b** bond 2 directions

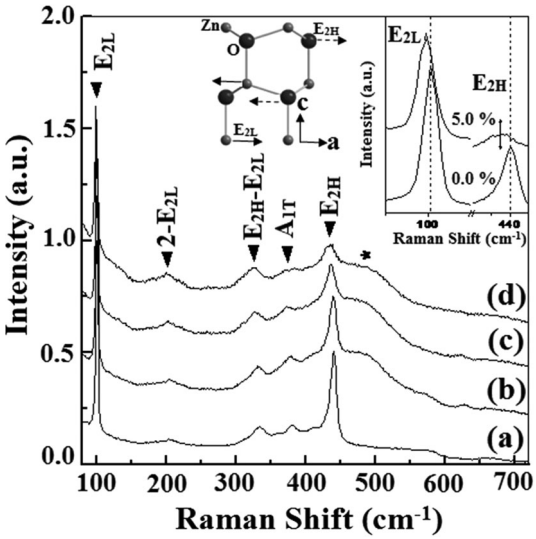

Fig. 7 Raman spectra of the *a* undoped, *b* 1.0, *c* 2.5, and *d* 5.0 mol% (nominal) Ga-doped samples. *Inset* detail of E_{2L} and E_{2H} Raman peaks of the undoped and the heaviest-doped samples. The scheme indicates the relative motion of Zn and O atoms in E_{2L} and E_{2H} phonon modes

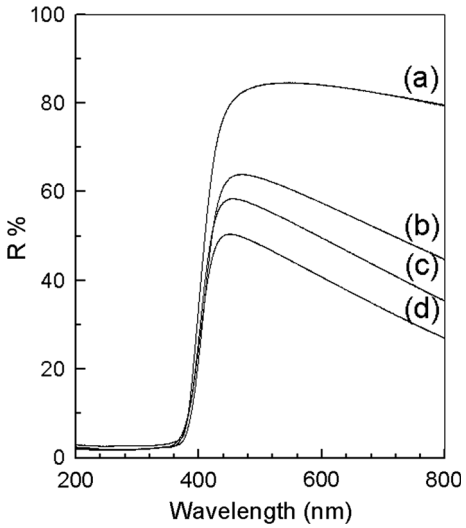

Fig. 8 Diffuse reflectance spectra of the *a* undoped, *b* 1.0, *c* 2.5, and *d* 5.0 mol% (nominal) Ga-doped samples

mode (O-sublattice). Since oxygen is less massive than zinc, it is expected that the redistribution of electron density due to gallium doping has a stronger influence on the oxygen sublattice. Such perturbation of oxygen environment is enhanced by the generation of point defects (like V_{Zn}) for preserving local neutrality [18]. In this regard, Bundesmann et al. [32] observed quenching of E_{2H} Raman peak in their doped ZnO samples, regardless of the doping atom identity (Fe, Sb, Al, and Ga). Therefore, changes of the E_{2H} Raman peak of ZnO could be used as sign of effective doping.

Obtained MEM results indicate that the redistribution of electron density is induced by Ga atoms located at Zn sites. Such a change in lattice-site environment due to incorporation of the electronic impurities causes a breakdown of translational symmetry of ZnO lattice as Raman spectroscopy reveals. If the Ga atoms incorporated mainly as substitutional defects, then we can expect a large density of extra valence electrons, which is capable of modifying the optical properties of ZnO nanostructures. Therefore, optical spectroscopies can provide valuable information in this regard.

The diffuse reflectance spectra of the doped and undoped samples are shown in Fig. 8. All the samples revealed an abrupt decrease of reflectance at the UV region related with the band edge absorption. It is interesting to note that as the Ga content increases, the reflectance in the visible region diminishes notoriously, possibly due to the incorporation of defect levels in the forbidden energy gap and formation of band tails [35]. The estimated band gap energy (E_g) and band-tail parameter (E_0) for each sample applying the K–M (Kubelka–Munk) formalism [36] and the Halperin–Lax theory [37], respectively, are summarized in Table 1. As can be seen, the increase of Ga content results in a slight increase of E_g, which can be attributed to the Burstein–Moss shift [38–40], the values of E_0 (see Table 1) support this assumption. In this regard, it has been demonstrated that higher values of band-tail parameter correspond to higher carrier concentrations [41].

Conclusions

Through hydrothermal process, one-dimensional ZnO nanostructures with different Ga contents could be grown. Our results indicate that the incorporated Ga atoms basically introduce into the ZnO lattice by substituting Zn atoms. Due to the substitution of divalent Zn atoms by trivalent Ga atoms, the charge density around the lattice sites gets modified. It has been observed that the redistribution of electron density induced by Ga doping is not isotropic. On increasing the Ga content, while the Zn–O bond disposed along the *c*-axis gets more ionic, the lateral Zn–O bond (108° to the *c*-axis) acquires a mixed ionic-covalent character. The effect of electron redistribution around the lattice sites also affects the vibrational and optical properties of the ZnO nanostructures. A large incorporation of Ga_{Zn} defects modifies strongly the lattice dynamics and increases the carrier concentration of the ZnO nanostructutres, inducing the formation of band tails into the forbidden band gap.

Acknowledgements This work was supported by the CONACyT, Mexico (Grants# CB-2010/151767 & CB-2011/168027) and VIEP-BUAP. The authors are also grateful to the Madura College, Tamil Nadu, India and SAIF, Cochin University, India for extending their experimental facilities.

References

1. Hong CS, Park HH, Moon J, Park HH (2006) Effect of metal (Al, Ga, and In)-dopants and/or Ag-nanoparticles on the optical and electrical properties of ZnO thin films. Thin Solid Films 515:957–960
2. Bethke S, Pan H, Wessels B (1988) Luminescence of hetero-epitaxial zinc oxide. Appl Phys Lett 52:138–140
3. Choopun S, Vispute RD, Woch W, Balsamo A, Sharma RP, Venkatesan T, Iliadis A, Look DC (1999) Oxygen Pressure-tuned epitaxy and optoelectronic properties of laser-deposited ZnO films on sapphire. Appl Phys Lett 75:3947–3949
4. Wenas WW, Yamada A, Takahashi K, Yoshino M, Konagai M (1991) Electrical and optical properties of boron-doped ZnO thin films for solar cells grown by metal organic chemical vapor deposition. J Appl Phys 70:7119–7123
5. Agura H, Suzuki A, Matsushita T, Aoki T, Okuda M (2003) Low resistivity transparent conducting Al-doped ZnO films prepared by pulsed laser deposition. Thin Solid Films 445:263–267
6. Ko HJ, Chen YF, Hong SK, Wenisch H, Yao T, Look DC (2000) Ga-doped ZnO films grown on GaN templates by plasma-assisted molecular-beam epitaxy. Appl Phys Lett 77:3761–3763
7. Hu J, Gordon RG (1993) Electrical and optical properties of indium doped zinc oxide films prepared by atmospheric pressure chemical vapor deposition. Mater Res Soc Symp Proc 283:891–896
8. Minami T (2005) Transparent conducting oxide semiconductors for transparent electrodes. Semicond Sci Technol 20:S35–S44
9. Gabás M, Landa-Cánovas A, Costa-Krämer J, Agulló-Rueda F, González-Elipe AR, Díaz-Carrascp P, Hernández-Moro J, Lorite I, Herrero P, Castillero P, Barranco A, Ramon Ramos-Barrado J (2013) Differences in n-type doping efficiency between Al– and Ga–ZnO films. J Appl Phys 113:9–163709
10. Xu C, Kim M, Chun J, Kim D (2005) Growth of Ga-doped ZnO nanowires by two-step vapor phase method. Appl Phys Lett 86:3–133107
11. Özgür Ü, Hofstetter D, Morkoc H (2010) ZnO devices and applications: a review of current status and future prospects. Proc IEEE 98:1255–1268
12. Ahmad M, Zhu J (2011) ZnO based advanced functional nano-structures: synthesis, properties and applications. J Mater Chem 21:599–614
13. Djurišić AB, Chen XY, Leung YH, Ng AMC (2012) ZnO nanostructures: growth, properties and applications. J Mater Chem 22:6526–6535
14. Rietveld HM (1969) A profile refinement method for nuclear and magnetic structures. J Appl Crystallogr 2:65–71
15. McCusker LB, Von Dreele RB, Cox DE, Loüer D, Scardi P (1999) Rietveld refinement guidelines. J Appl Crystallogr 32: 36–50
16. Kumazawa S, Kubota Y, Takata M, Sakata M, Ishibashi Y (1993) MEED: a program package for electron density distribution calculation by the maximum entropy method. J Appl Crystallogr 26:453–457
17. Pineda-Hernandez G, Escobedo-Morales A, Pal U, Chigo-Anota E (2012) Morphology evolution of hydrothermally grown ZnO nanostructures on gallium doping and their defect structures. Mater Chem Phys 135:810–817
18. West AR (1984) Solid state chemistry and its applications. Wiley, Great Britain
19. ICDD (1997) Joint committee powder diffraction standards, Card No. 36-1451, version 1.30, Database of the international center for diffraction data, 12, campus boulevard, Newton square, Pennsylvania, 19073-3273, USA
20. Yoon MH, Lee SH, Park HL, Kim HK, Jang MS (2002) Solid solubility limits of Ga and Al in ZnO. J Mater Sci Lett 21:1703–1704
21. Wang R, Sleight AW, Cleary D (1996) High conductivity in Ga doped ZnO powders. Chem Mater 8:433–439
22. Petříček V, Dušek M, Palatinus L (2006) Jana 2006: The crystallographic computing system. Institute of Physics, Praha
23. Hahn T (2005) International tables for crystallography. Space group symmetry, vol A. Springer, The Netherlands
24. Özgür Ü, Alivov YI, Liu C, Teke A, Reshchikov MA, Dogan S, Avrutin V, Cho SJ, Morkoc H (2005) A comprehensive review of ZnO materials and devices. J Appl Phys 98:103–041301
25. Sheu JK, Shu KW, Lee ML, Tun CJ, Chi GC (2007) Effect of thermal annealing on Ga-doped ZnO films prepared by magnetron sputtering. J Electrochem Soc 154:H521–H524
26. Saravanan R (2008) Grain software. Private communication
27. Guinier A (1994) X-ray diffraction in crystals, imperfect crystals and amorphous bodies. Dover Publications, New York
28. Izumi F, Dilanian RA (2002) Recent research developments in physics, Part II, vol 3. Transworld Research Network, Trivandrum
29. Momma K, Izumi F (2011) VESTA 3 for three-dimensional visualization of crystal, volumetric and morphology data. J Appl Crystallogr 44:1272–1276
30. Hardcastle FD, Wachs IE (1991) Determination of vanadium–oxygen bond distances and bond orders by Raman spectroscopy. J Phys Chem 95:5031–5041
31. Dong S, Padmakumar R, Banerjee R, Spiro TG (1996) Resonance Raman Co–C stretching frequencies reflect bond strength changes in alkyl cobalamins, but are unaffected by trans-ligand substitution. J Am Chem Soc 118:9182–9183
32. Bundesmann C, Ashkenov N, Schubert M, Spemann D, Butz T, Kaidashev EM, Lorenz M, Grundmann M (2003) Raman scattering in ZnO thin films doped with Fe, Sb, Al, Ga and Li. Appl Phys Lett 83:1974–1976
33. Wang X, Xu J, Yu X, Xue K, Yu J, Zhao X (2007) Structural evidence of secondary phase segregation from the Raman vibrational modes in $Zn_{1-x}Co_xO$ ($0 < x < 0.6$). Appl Phys Lett 91:3–031908
34. Windisch CF, Exarhos GJ, Owings RR (2004) Vibrational spectroscopic study of the site occupancy distribution of cations in nickel cobalt oxides. J Appl Phys 95:5435–5442
35. Holland TJB, Redfern SAT (1997) Unit cell refinement from powder diffraction data: the use of regression diagnostics. Mineral Mag 61:65–77
36. Escobedo-Morales A, Sánchez Mora E, Pal U (2007) Use of diffuse reflectance spectroscopy for optical characterization of un-supported nanostructures. Rev Mex Fis S53:18–22
37. Halperin BI, Lax M (1966) Impurity-band tails in the high-density limit. I. Minimum counting methods. Phys Rev 148:722–740
38. Burstein E (1954) Anomalous optical absorption limit in InSb. Phys Rev 93:632–633
39. Moss TS (1954) The interpretation of the properties of indium antimonide. Proc Phys Soc London B 76:775–782
40. Wang R, King LLH, Sleight AW (1996) Highly conducting transparent thin films based on zinc oxide. J Mater Res 11:1659–1664
41. Iribarren A, Castro-Rodríguez R, Sosa V, Peña JL (1998) Band-tail parameter modeling in semiconductor materials. Phys Rev B 58:1907–1911